Microlensing Binaries Discovered through High-Magnification Channel

I.-G. Shin[1], J.-Y. Choi[1], S.-Y. Park[1], C. Han[1,72,79], A. Gould[9,72], T. Sumi[30,73], A. Udalski[31,74], J.-P. Beaulieu[34,75], M. Dominik[47,76,77,78],

and

W. Allen[2], M. Bos[3], G.W. Christie[4], D.L. Depoy[5], S. Dong[6], J. Drummond[7], A. Gal-Yam[8], B.S. Gaudi[9], L.-W. Hung[10], J. Janczak[11], S. Kaspi[12], C.-U. Lee[13], F. Mallia[14] D. Maoz[12], A. Maury[14], J. McCormick[15], L.A.G. Monard[16], D. Moorhouse[17], J. A. Muñoz[18], T. Natusch[4], C. Nelson[19], B.-G. Park[13], R.W. Pogge[9], D. Polishook[12], Y. Shvartzvald[12], A. Shporer[12], G. Thornley[17], J.C. Yee[9]

(The µFUN Collaboration),

F. Abe[20], D.P. Bennett[21], I.A. Bond[22], C.S. Botzler[23], A. Fukui[20], K. Furusawa[20], F. Hayashi[20], J.B. Hearnshaw[24], S. Hosaka[20], Y. Itow[20], K. Kamiya[20], P.M. Kilmartin[25], S. Kobara[20], A. Korpela[26], W. Lin[22], C.H. Ling[22], S. Makita[20], K. Masuda[20], Y. Matsubara[20], N. Miyake[20], Y. Muraki[27], M. Nagaya[20], K. Nishimoto[20], K. Ohnishi[28], T. Okumura[20], K. Omori[20], Y.C. Perrott[23], N. Rattenbury[23], To. Saito[29], L. Skuljan[22], D.J. Sullivan[26], D. Suzuki[30], W.L. Sweatman[22], P.J. Tristram[25], K. Wada[30], P.C.M. Yock[23]

(The MOA Collaboration),

M.K. Szymański[31], M. Kubiak[31], G. Pietrzyński[31,32], I. Soszyński[31], R. Poleski[31], K. Ulaczyk[31], Ł. Wyrzykowski[31,33], S. Kozłowski[31], P. Pietrukowicz[31]

(The OGLE Collaboration)

M.D. Albrow[24], V. Batista[9], D.M. Bramich[46], S. Brillant[35], J.A.R. Caldwell[69], J.J. Calitz[71], A. Cassan[34], A. Cole[36], K.H. Cook[70], E. Corrales[34], Ch. Coutures[34], S. Dieters[34,37], D. Dominis Prester[38], J. Donatowicz[39], P. Fouqué[37], J. Greenhill[36], M. Hoffman[71], U.G. Jørgensen[60,61], S. R. Kane[40], D. Kubas[34,35], J.-B. Marquette[34], R. Martin[44], P. Meintjes[71], J. Menzies[41], K.R. Pollard[24], K. C. Sahu[42], J. Wambsganss[43], A. Williams[44], C. Vinter[60], M. Zub[43]

(The PLANET Collaboration)

A. Allan[45], P. Browne[47], K. Horne[47], C. Snodgrass[48,35], I. Steele[49], R. Street[50], Y. Tsapras[50]

(The RoboNet Collaboration)

and

K.A. Alsubai[51], V. Bozza[52], P. Browne[47], M.J. Burgdorf[53,54], S. Calchi Novati[52,55], P. Dodds[47], S. Dreizler[56], F. Finet[57], T. Gerner[58], M. Glitrup[59], F. Grundahl[59], S. Hardis[60], K. Harpsøe[60,61], F.V. Hessman[56], T.C. Hinse[13,60,62], M. Hundertmark[47,56], N. Kains[47,63], E. Kerins[64], C. Liebig[47,58], G. Maier[58], L. Mancini[52,65], M. Mathiasen[60], M.T. Penny[64], S. Proft[58], S. Rahvar[66], D. Ricci[57], G. Scarpetta[52,67], S. Schäfer[56], F. Schönebeck[58], J. Skottfelt[60], J. Surdej[57], J. Southworth[68], F. Zimmer[58]

(The MiNDSTEp Consortium)

[1]Department of Physics, Institute for Astrophysics, Chungbuk National University, Cheongju 371-763, Korea

[2]Vintage Lane Observatory, Blenheim, New Zealand

[3]Molehill Astronomical Observatory, North Shore, New Zealand

[4]Auckland Observatory, P.O. Box 24-180, Auckland, New Zealand

[5]Department of Physics, Texas A&M University, College Station, TX, USA

[6]Institute for Advanced Study, Einstein Drive, Princeton, NJ 08540, USA

[7]Possum Observatory, Patutahi, New Zealand

[8]Benoziyo Center for Astrophysics, the Weizmann Institute, Israel

[9]Department of Astronomy, Ohio State University, 140 W. 18th Ave., Columbus, OH 43210, USA

[10]Department of Physics & Astronomy, University of California Los Angeles, Los Angeles, CA 90095, USA

[11]Department of Physics, Ohio State University, 191 W. Woodruff, Columbus, OH 43210, USA

[12]School of Physics and Astronomy, Tel-Aviv University, Tel Aviv 69978, Israel

[13]Korea Astronomy and Space Science Institute, Daejeon 305-348, Korea

[14]Campo Catino Austral Observatory, San Pedro de Atacama, Chile

[15]Farm Cove Observatory, Pakuranga, Auckland

[16]Bronberg Observatory, Pretoria, South Africa

[17]Kumeu Observatory, Kumeu, New Zealand

[18]Departamento de Astronomiá y Astrofísica, Universidad de Valencia, E-46100 Burjassot, Valencia, Spain

[19]College of Optical Sciences, University of Arizona, 1630 E. University Blvd, Tucson Arizona, 85721, USA

[20]Solar-Terrestrial Environment Laboratory, Nagoya University, Nagoya, 464-8601, Japan

[21]Department of Physics, University of Notre Damey, Notre Dame, IN 46556, USA

[22]Institute of Information and Mathematical Sciences, Massey University, Private Bag 102-904, North Shore Mail Centre, Auckland, New Zealand

[23]Department of Physics, University of Auckland, Private Bag 92019, Auckland, New Zealand

[24]University of Canterbury, Department of Physics and Astronomy, Private Bag 4800, Christchurch 8020, New Zealand

[25]Mt. John Observatory, P.O. Box 56, Lake Tekapo 8770, New Zealand

[26]School of Chemical and Physical Sciences, Victoria University, Wellington, New Zealand

[27]Department of Physics, Konan University, Nishiokamoto 8-9-1, Kobe 658-8501, Japan

[28]Nagano National College of Technology, Nagano 381-8550, Japan

[29]Tokyo Metropolitan College of Industrial Technology, Tokyo 116-8523, Japan

[30]Department of Earth and Space Science, Osaka University, Osaka 560-0043, Japan

[31]Warsaw University Observatory, Al. Ujazdowskie 4, 00-478 Warszawa, Poland

[32]Universidad de Concepción, Departamento de Fisica, Casilla 160-C, Concepción, Chile

[33]Institute of Astronomy Cambridge University, Madingley Road, CB3 0HA Cambridge, UK

[34]Institut d'Astrophysique de Paris, UMR7095 CNRS–Université Pierre & Marie Curie, 98 bis boulevard Arago, 75014 Paris, France

[35]European Southern Observatory, Casilla 19001, Vitacura 19, Santiago, Chile

[36]School of Math and Physics, University of Tasmania, Private Bag 37, GPO Hobart, Tasmania 7001, Australia

[37]LATT, Université de Toulouse, CNRS, 14 Avenue Edouard Belin, 31400 Toulouse, France

[38]Physics Department, Faculty of Arts and Sciences, University of Rijeka, Omladinska 14, 51000 Rijeka, Croatia

[39]Technical University of Vienna, Department of Computing, Wiedner Hauptstrasse 10, Vienna, Austria

[40]NASA Exoplanet Science Institute, Caltech, MS 100-22, 770 South Wilson Avenue, Pasadena, CA 91125, USA

[41]South African Astronomical Observatory, P.O. Box 9 Observatory 7935, South Africa

[42]Space Telescope Science Institute, 3700 San Martin Drive, Baltimore, MD 21218, USA

[43]Astronomisches Rechen-Institut (ARI), Zentrum für Astronomie der Universität Heidelberg (ZAH), Mönchhofstrasse 12-14, 69120 Heidelberg, Germany

[44]Perth Observatory, Walnut Road, Bickley, Perth 6076, Australia

[45]School of Physics, University of Exeter, Stocker Road, Exeter, Devon, EX4 4QL, UK

[46]European Southern Observatory, Karl-Schwarzschild-Straße 2, 85748 Garching bei München, Germany

[47]School of Physics & Astronomy, SUPA, University of St. Andrews, North Haugh, St. Andrews, KY16 9SS, UK

[48]Max-Planck-Institut för Sonnensystemforschung, Max-Planck-Str. 2, 37191 Katlenburg-Lindau, Germany

[49]Astrophysics Research Institute, Liverpool John Moores University, Egerton Wharf, Birkenhead CH41 1LD, UK

[50]Las Cumbres Observatory Global Telescope Network, 6740B Cortona Dr, Suite 102, Goleta, CA 93117, USA

[51]Qatar Foundation, P.O. Box 5825, Doha, Qatar

[52]Università degli Studi di Salerno, Dipartimento di Fisica "E.R. Caianiello", Via S. Allende, 84081 Baronissi (SA), Italy

[53]Deutsches SOFIA Institut, Universität Stuttgart, Pfaffenwaldring 31, 70569 Stuttgart, Germany

[54]SOFIA Science Center, NASA Ames Research Center, Mail Stop N211-3, Moffett Field CA 94035, USA

[55]Istituto Internazionale per gli Alti Studi Scientifici (IIASS), Vietri Sul Mare (SA), Italy

[56]Institut für Astrophysik, Georg-August-Universität, Friedrich-Hund-Platz 1, 37077 Göttingen, Germany

[57]Institut d'Astrophysique et de Géophysique, Allée du 6 Août 17, Sart Tilman, Bât. B5c, 4000 Liège, Belgium

[58]Astronomisches Rechen-Institut, Zentrum für Astronomie der Universität Heidelberg (ZAH), Mönchhofstr. 12-14, 69120 Heidelberg, Germany

[59]Department of Physics & Astronomy, Aarhus Universitet, Ny Munkegade, 8000 Århus C, Denmark

[60]Niels Bohr Institute, University of Copenhagen, Juliane Maries vej 30, 2100 Copenhagen, Denmark

[61]Centre for Star and Planet Formation, Geological Museum, Øster Voldgade 5, 1350 Copenhagen, Denmark

[62]Armagh Observatory, College Hill, Armagh, BT61 9DG, Northern Ireland, UK

[63]ESO Headquarters, Karl-Schwarzschild-Str. 2, 85748 Garching bei München, Germany

[64]Jodrell Bank Centre for Astrophysics, University of Manchester, Oxford Road,Manchester, M13 9PL, UK

[65]Max Planck Institute for Astronomy, Königstuhl 17, 619117 Heidelberg, Germany

[66]Department of Physics, Sharif University of Technology, P. O. Box 11155–9161, Tehran, Iran

[67]INFN, Gruppo Collegato di Salerno, Sezione di Napoli, Italy

[68]Astrophysics Group, Keele University, Staffordshire, ST5 5BG, UK

[69]McDonald Observatory, 16120 St Hwy Spur 78 #2, Fort Davis, TX 79734, USA

[70]Institute of Geophysics and Planetary Physics (IGPP), L-413, Lawrence Livermore National Laboratory, PO Box 808,

ABSTRACT

Microlensing can provide a useful tool to probe binary distributions down to low-mass limits of binary companions. In this paper, we analyze the light curves of 8 binary lensing events detected through the channel of high-magnification events during the seasons from 2007 to 2010. The perturbations, which are confined near the peak of the light curves, can be easily distinguished from the central perturbations caused by planets. However, the degeneracy between close and wide binary solutions cannot be resolved with a 3σ confidence level for 3 events, implying that the degeneracy would be an important obstacle in studying binary distributions. The dependence of the degeneracy on the lensing parameters is consistent with a theoretic prediction that the degeneracy becomes severe as the binary separation and the mass ratio deviate from the values of resonant caustics. The measured mass ratio of the event OGLE-2008-BLG-510/MOA-2008-BLG-369 is $q \sim 0.1$, making the companion of the lens a strong brown-dwarf candidate.

Subject headings: gravitational lensing: micro – binaries: general

1. Introduction

Microlensing can be used to probe the distributions of binary companions of Galactic stars as functions of mass ratio and separation, which provide important observational constraints on theories of star formation. Being sensitive to low-mass companions that are difficult to be detected by other methods, microlensing enables to make complete distributions down to the low mass limit of binary companions (Gould 2001).

Despite the importance, the progress of this application of microlensing to the statistical analysis of binaries has been stagnant. There are two main reasons for this. The first reason arises due to the difficulties in estimating the detection efficiency of binary lenses. Previously, lensing events caused by binary lenses were mainly detected through accidental detections of sudden rises and falls of the source flux resulting from source crossings over caustics formed by binary lenses, e.g. Udalski et al. (1994), Alcock et al. (2000), Jaroszyński, et al. (2004, 2006, 2010), and Skowron et al. (2007). The caustics represent the positions on the source plane at which the lensing magnification of a point source becomes infinite. For binary events detected through this channel, it is difficult to estimate the detection efficiency due to the haphazard nature

Livermore, CA 94551, USA

[71]University of the Free State, Faculty of Natural and Agricultural Sciences, Department of Physics, PO Box 339, Bloemfontein 9300, South Africa

[72]The μFUN Collaboration

[73]The MOA Collaboration

[74]The OGLE Collaboration

[75]The PLANET Collaboration

[76]The RoboNet Collaboration

[77]The MiNDSTEp Consortium

[78]Royal Society University Research Fellow

[79]Corresponding author

of caustic crossings. The second reason is that microlensing is mainly sensitive to binaries distributed over a narrow range of separations. The probability of caustic crossings increases with the increase of the caustic size. The caustic size becomes maximum when the separation between the lens components is of order the Einstein radius, $\theta_{\rm E}$, and decreases rapidly with the increase or decrease of the separation from $\theta_{\rm E}$. As a result, the majority of microlensing binaries have separations distributed within a small range. This limits especially the study of the distribution of binary separations.

However, under the current observational strategy of microlensing experiments focusing on planet detections, a significant fraction of binary events are detected through a new channel of high-magnification events. For the detections of short-duration planetary signals in lensing light curves, planetary lensing experiments are being conducted in survey and follow-up mode, where alerts of ongoing events are issued by survey experiments and intensive observations of these events are conducted by follow-up experiments. In this mode, high-magnification events are the most important targets for follow-up observations because the source trajectories of these events always pass close to the central perturbation region induced by the planet and thus the efficiency of planet detections is very high (Griest & Safizadeh 1998). In addition, the time of the perturbation can be predicted in advance and thus intensive follow-up can be prepared. This leads to an observational strategy of intensively monitoring all high-magnification events regardless of whether they show signals of planets.

In addition to planets, high-magnification events are sensitive to binaries as well, especially those with separations substantially smaller (close binaries) or larger (wide binaries) than the Einstein radius. For close binaries, there exist three caustics where one is formed around the center of mass of the binary and the other two are located away from the barycenter. For wide binaries, on the other hand, there exist two caustics each of which is located adjacent to the individual lens components. Then, high-magnification events resulting from the source trajectories passing either close to the center of mass of a close binary or one of the components of a wide binary are sensitive to binaries. The high sensitivity to close and wide binaries combined with the strategy of monitoring all high-magnification events imply that binary events detected through the high-magnification channel are important for the construction of an unbiased sample of binaries with a wider range of separations and thus for the statistical studies of binaries (Han 2009).

In this paper, we analyze the light curves of 8 binary microlensing events detected through the high-magnification channel during the seasons from 2007 to 2010. We search for the solutions of binary lensing parameters by conducting modeling of the light curves. We discuss the characteristics of the binaries.

2. Observation

All 8 tested events analyzed in this work were detected toward the Galactic bulge direction. In Table 1, we list the coordinates of the events. Each event is designated first by the microlensing group who first discovered the event and then followed by the year when the event was discovered. If an event is discovered independently by two different groups, they are named separately. For example, the event OGLE-2008-BLG-510/MOA-2008-BLG-368 was discovered by both OGLE and MOA groups in 2008. For all events, the peak magnifications are high and thus they are issued as important targets for follow-up observations by the MOA (Bond et al. 2001; Sumi et al. 2003) and OGLE (Udalski 2003) survey experiments. As a result, the peaks of the light curves were densely covered by follow-up observations including the μFUN (Gould et al. 2006), PLANET (Beaulieu et al. 2006), RoboNet (Tsapras et al. 2009), and MiNDSTEp (Dominik et al. 2010). In Table 2, we list the survey and follow-up groups who participated in the observation of the individual events.

In Table 3, we also list the telescopes used for observations along with their locations.

The photometry of the data was conducted by using the codes developed by the individual groups. For some events, we re-reduced data based on the image subtraction method to ensure better photometry. The error bars of the data sets were rescaled so that χ^2/dof becomes unity for the data set of each observatory where χ^2 is computed based on the best-fit model.

In Figure 1 – 8, we present the light curves of the individual events. For all events, the common feature of the light curves is that most of the light curve is consistent with the standard single-lens light curve (Paczyński 1986) and the perturbation is confined in a narrow region around the peak.

3. Modeling

For the light curve of each event, we search for solutions of lensing parameters in the space encompassing both stellar and planetary companions. The light curve of a binary-lens event is characterized by 6 basic parameters. The first 3 parameters are related to the geometry of the lens-source approach. They are the Einstein time scale, t_{E}, the time of the closest lens-source approach, t_0, and the lens source separation at that moment, u_0. The other 3 parameters are related to the binarity of the lens. These parameters are the mass ratio between the lens components, q, the projected separation in units of the Einstein radius, s, and the angle between the source trajectory and the binary axis, α. For all tested events, the perturbations exhibit features caused either by crossings over or approaches close to caustics and thus it is required to consider the modification of magnifications caused by the finite-source effect during the perturbation. This requires to include an additional parameter of the normalized source radius, $\rho_\star$, which is related to the angular source radius, $\theta_\star$, and the Einstein radius by $\rho_\star = \theta_\star/\theta_{\mathrm{E}}$.

For each event, we search for the solution of the best-fit parameters by minimizing χ^2 in the parameter space. We do this by dividing the parameters into two categories. For the parameters in the first category, grid searches are conducted. For the remaining parameters in the second category are searched by using a downhill approach. We choose s, q, and α as the grid parameters because these parameters are related to the features of lensing light curves in a complicated pattern while the other parameters are more directly related to the features of the light curve. For the χ^2 minimization, we use a Markov Chain Monte Carlo method. Brute-force search over the space of the grid parameters is needed in order to investigate possible local minima of degenerate solutions. This is important because it is known that there exists a pair of close/wide solution for binary-lens events, especially for binaries with separations substantially smaller or larger than the Einstein radius (Dominik 1999). Once local minima are identified, we check all of them by gradually narrowing down the grid parameter space. When the space is sufficiently confined, we allow the grid parameters to vary in order to pin down the exact location of the solution.

Computation of magnifications affected by the finite-source effect is based on the ray-shooting method (Schneider & Weiss 1986; Kayser et al. 1986; Wambsganss 1997). In this numerical method, rays are uniformly shot from the image plane, bent according to the lens equation, and land on the source plane. Then, the finite magnification is computed by comparing the number densities of rays on the image and source planes. This method requires heavy computation because a large number of rays are needed for accurate magnification computation. We accelerate the computation by using two major methods. The first method is applying the "map making" method (Dong et al. 2006). In this method, a map for a given set of (s, q) is used to produce numerous light curves resulting from different source trajectories instead of shooting rays all over again. The second method is applying the semi-analytic hexadecapole approximation (Pejcha & Heyrovský

2009; Gould 2008) for the finite magnification computation when the source is not very close to the caustic.

In computing finite magnifications, we consider the effect of limb-darkening of the source star surface by modeling the surface brightness by

$$S_\lambda = \frac{F_\lambda}{\pi\theta_\star^2}\left[1 - \Gamma_\lambda\left(1 - \frac{3}{2}\cos\phi\right)\right] \tag{1}$$

where Γ_λ is the linear limb-darkening coefficient, F_λ is the flux from the source star, and ϕ is the angle between the line of sight toward the source star and the normal to the source star's surface. We choose the coefficients from Claret (2000), where the source type is determined from the location of the source star on the color-magnitude diagram. In Table 4, we present the coefficients of the individual events.

In addition to the modeling based on standard binary-lensing parameters, we conduct modeling considering the second-order effects on the light curve. The first effect is the "parallax effect" that is caused by the change of the observer position induced by the orbital motion of the Earth around the Sun (Gould 1992; Alcock et al. 1995). The second effect is the "orbital effect" caused by the change of the lens position induced by the orbital motion of the lens (Albrow et al. 2002; Shin et al. 2011; Skowron et al. 2011). Measurement of the parallax effect is important because it allows to determine the physical parameters of the lens system (Gould 1992). Detecting the orbital effect is important because it can help to characterize the orbital parameters of the lens system.

4. Results

In Table 5, we present the best-fit parameters found from modeling. For each event, we present the pair of close and wide binary solutions in order to show the severity of the degeneracy. The best-fit light curves of the individual events are overplotted on the data in Figure 1 – 8. In Figure 9, we also present the geometry of the lens systems. For each event, we present two sets of geometry corresponding to the close (left panel) and wide (right panel) binary solutions. In each panel, the big and small dots represent the locations of the binary lens components with heavier and lighter masses, respectively. The closed figure with cusps represents the caustic and the straight line with an arrow represents the source trajectory with respect to the caustic. The empty circle near the tip of the arrow on the source trajectory represents the source size. The dashed circle represents the Einstein ring. For the close binary, there exists a single Einstein ring whose radius corresponds to the total mass of the binary. For the wide binary, on the other hand, there exist two rings with radii corresponding to the masses of the individual lens components. The small panel on the right side of each main panel shows the enlargement of the region around the caustic. We find that the perturbations of the events MOA-2008-BLG-159, MOA-2009-BLG-408, MOA-2010-BLG-349, and MOA-2010-BLG-546 were produced by the source star's crossing over the central caustic. For the events MOA-2007-BLG-146, OGLE-2008-BLG-510/MOA-2008-BLG369, MOA-2010-BLG-266, and MOA-2010-BLG-406, on the other hand, the perturbations were produced by the approach of the source trajectory close to one of the cusps of the central caustic.

We find that the modeling including the parallax and orbital effects does not yield solutions with statistically significant χ^2 improvement. Considering that the range of the time scales of the events is 5 days $\lesssim t_{\rm E} \lesssim$ 30 days, we judge that the difficulties in detecting the second-order effects are due to the short time scales of the events. Since the lens parallaxes are not measured, we are not able to determine the physical parameters of lenses. However, for 5 events we are able to measure the Einstein radii, which is another quantity to constrain the physical lens parameters. The Einstein radius is measured from the

deviation of the light curve caused by the finite-source effect. By detecting the deviation, the normalized source radius $\rho_\star$ is measured from modeling. With the additional information of the source radius, which is obtained from the location of the source star on the color-magnitude diagram of stars in the field around the source star, the Einstein radius is determined as $\theta_{\rm E} = \theta_\star / \rho_\star$ (Yoo et al. 2004). With the measured Einstein radius, the relative lens-source proper motion is determined by $\mu = \theta_{\rm E}/t_{\rm E}$. The values of the measured Einstein radii and the proper motions are presented in Table 5. Among the 5 events for which the Einstein radius is measured, 4 events are caustic-crossing events. For the case of MOA-2007-BLG-146, the center of the source star did not cross the caustic but the edge of the source passed over the caustic and thus the Einstein radius was measurable.

It is known that central perturbations, which are the common features for all analyzed events, can be produced either by planetary companions or binaries (Albrow et al. 2002; Han & Gaudi 2008; Han 2009; Han & Kim 2009). We find that the planet/binary degeneracy is easily distinguished and the binary origin can be firmly identified. The range of the mass ratios is $0.1 \lesssim q \lesssim 0.73$.[1] We note that the event OGLE-2008-BLG-510/MOA-2008-BLG-369 is caused by a binary with a low-mass companion. Although the absolute value of the lens mass cannot be determined, the measured mass ratio $q \sim 0.1$ makes the companion of the binary a brown-dwarf candidate considering that the time scale of the event $t_{\rm E} \sim 27$ days is a typical one for Galactic bulge events caused by low-mass stars. Therefore, this event demonstrates that microlensing is a useful tool to study low-mass binary companions including brown dwarfs. By the time of completing this paper, we learned that Bozza et al. (2011) released the result of analysis for OGLE-2008-BLG-510/MOA-2008-BLG-369. Their result is very consistent with ours and stated the possibility of the brown dwarf companion.

Although the binary nature of the lenses is clearly identified, it is found that the degeneracy between the close and wide binary solutions is severe for some events. The close/wide binary degeneracy, which results from a symmetry in the lens equation, was first mentioned by Griest & Safizadeh (1998) and further investigated by Dominik (1999). The events for which the degeneracy cannot be distinguished with a 3σ confidence level include OGLE-2008-BLG-510/MOA-2008-BLG-369, MOA-2009-BLG-408, and MOA-2010-BLG-546. The severity of the degeneracy and the correspondence in the lens-system geometry between the pairs of degenerate solutions can be seen from the comparison of the geometry of the lens system at the time of perturbation. As predicted by theoretical studies, the close/wide degeneracy is caused by the similarity of the shape between the caustics of the close and wide binaries The caustic shape results from the combination of the projected separation and mass ratio. To see how the severity of the degeneracy depends on these parameters, we plot the locations of the degenerate solutions in the parameter space of s and q in Figure 10. In the plot, the filled dots denote that the degeneracy is resolved at the 3σ confidence level and the empty dots symbolize that the degeneracy is not resolved. The area encompassed by dashed lines represents the region within which the lens forms a single merged large caustic (resonant caustic). From the plot, it is found that the degeneracy becomes severe as the binary separation is located well away from the range of resonant caustics. Therefore, the degeneracy would be an important obstacle in studying binary distributions for binaries with very close or wide separations.

---

[1]In Table 5, the value of the mass ratio $q > 1$ represents the case where the source trajectory approaches the lighter component of the binary.

5. Conclusion and Discussion

We conducted modeling of light curves of 8 binary lensing events detected through the high-magnification channel during 2007 – 2010 seasons. We found that the binary/planet degeneracy of the central perturbations were easily distinguished. However, the degeneracy between the close and wide binary solutions could not be resolved with confidence for some of the events. We confirmed the theoretic prediction that the degeneracy becomes severe for binaries with separations substantially smaller or wider than the Einstein radius and thus the close/wide degeneracy would be an important obstacle in the studies of binary distributions. For one of the events, the measured mass ratio is in the range of a brown dwarf, demonstrating that microlensing is a useful tool to study low-mass binary companions.

Although it is difficult to draw meaningful statistical properties of binaries based on the handful events analyzed in this work, it is expected that the microlensing use of binary statistics would expand. One way for this improvement is the removal of human intervention in the selection process of a follow-up campaign. An example of this effort is the SIGNALMEN anomaly detector achieved by the ARTEMiS system (Dominik et al. 2007). Another way is conducting high-cadence surveys to dispense with follow-up observations. Recently, the OGLE group significantly increased the observational cadence by upgrading its camera with a wider field of view to the level of being able to detect short planetary perturbations by the survey itself. The Korea Microlensing Telescope Network (KMTNet) is a planned survey experiment that will achieve 10 minute sampling of all lensing events by using a network of 1.6 m telescopes to be located in three different continents in the Southern hemisphere with wide-field cameras. These new type surveys will enable not only to densely cover events but also to significantly increase the number of events in binary samples. Being able to detect and densely cover binary events without human intervention combined with the increased number of events will enable microlensing to become a useful method to study binary statistics.

Even with the increase of the number of events and the improvement of the process of obtaining samples, it is still an important issue to resolve the close/wide degeneracy. Han et al. (1999) proposed that astrometric observation of the centroid motion of a lensed star by using a high-resolution instrument makes it possible to resolve the ambiguity of the photometric binary-lens fit for most accidentally degenerate cases. However, it is found that the close/wide binary degeneracy is so severe that it causes the image centroids of the wide and close solutions to follow a similar pattern of motion although the motions of the image centroid for the two degenerate cases are displaced from one another long after the event and thus the degeneracy can eventually be resolvable (Han & Gould 2000). In addition, this method requires space-based astrometric instrument and thus can not be applicable to events being detected by current lensing experiments. A class of events for which the degeneracy can be photometrically resolved are repeating events where the source trajectory passes both the central perturbation region of one of the binary components and the effective lensing region of the other binary component, e.g. OGLE-2009-BLG-092/MOA-2009-BLG-137 (Ryu et al. 2010). However, this method can be applicable to a small fraction of events. Therefore, devising a general method resolving this degeneracy would be crucial for the statistical binary studies of microlensing binaries.

REFERENCES

Albrow, M. D., et al. 2002, ApJ, 572, 1031

Alcock, C., et al. 1995, ApJ, 454, L125

Alcock, C., et al. 2000, ApJ, 541, 270

Beaulieu, J.-P., et al. 2006, Nature, 439, 437

Bond, I. A., et al. 2001, MNRAS, 327, 868

Bozza, V., et al. 2011, MNRAS, submitted

Claret, A. 2000, A&A, 363, 1081

Dominik, M. 1999, A&A, 349, 108

Dominik, M., et al. 2007, MNRAS, 380, 792

Dominik, M., et al. 2010, Astron. Machr., 331, 671

Dong, S., et al. 2009 ApJ, 642, 842

Gould, A. 1992, ApJ, 392, 442

Gould, A. 2001, PASP, 113, 903

Gould, A. 2008, ApJ, 681, 1593

Gould, A., et al. 2006, ApJ, 644, L37

Griest, K., & Safizadeh, N. 1998, ApJ, 500, 37

Han, C., Chun, M -S., & Chang, K. 1999, ApJ, 536, 406

Han, C., & Gould, A. 2000, ApJ, 538, 653

Han, C. 2009, ApJ, 691, L9

Han, C. 2009, ApJ, 707, 1264

Han, C., & Gaudi B. S. 2008, ApJ, 689, 53

Han, C., & Kim, D. 2009, ApJ, 693, 1835

Jaroszyński, M., et al. 2004, Acta Astron., 54, 103

Jaroszyński, M., et al. 2006, Acta Astron., 56, 307

Jaroszyński, M., et al. 2010, Acta Astron., 60, 197

Kayser, R., Refsdal, S., & Stabell, R. 1986, A&A, 166, 36

Paczyński, B. 1986, ApJ, 304, 1

Pejcha, O., & Heyrovský, D. 2009, ApJ, 690, 1772

Ryu, Y.-H., et al. 2010, ApJ, 723, 81

Schneider, P., & Weiss, A. 1986, A&A, 164, 237

Shin, I.-G., et al. 2011, ApJ, 735, 855

Skowron, J., et al. 2007, Acta Astron., 57, 281

Skowron, J., et al. 2011, ApJ, 738, 87

Sumi, T., et al. 2003, ApJ, 591, 204

Tsapras, Y., et al. 2009, Astron. Nachr., 330, 4

Udalski, A., Szymański, M., Mao, S., Di Stefano, R., Kałużny, J., Kubiak, M., Mateo, M., & Krzemiński, W. 1994, ApJ, 436, L103

Udalski, A. 2003, Acta Astron., 53, 291

Yoo, J., et al. 2004, ApJ, 603, 139

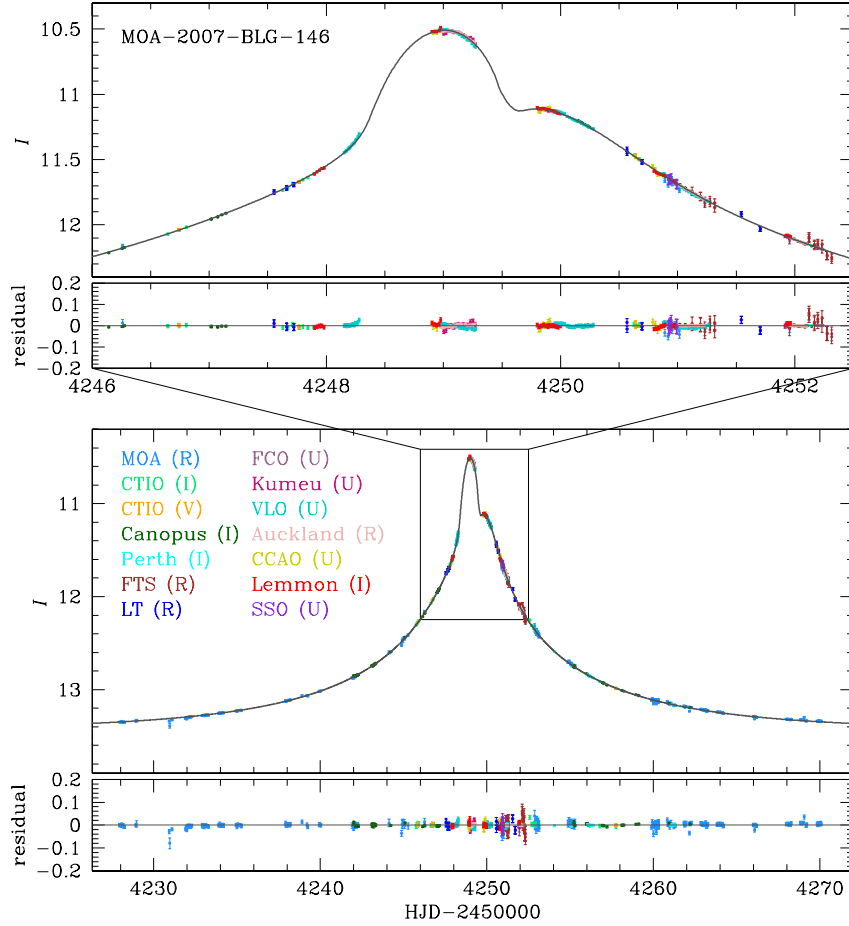Wambsganss, J. 1997, MNRAS, 284, 172

Fig. 1.— Light curve of the microlensing event MOA-2007-BLG-146. The upper panel shows the enlargement of the region around the peak. The lensing parameters and the lens-system geometry corresponding to the best-fit model light curve are presented in Table 5 and Fig. 10, respectively.
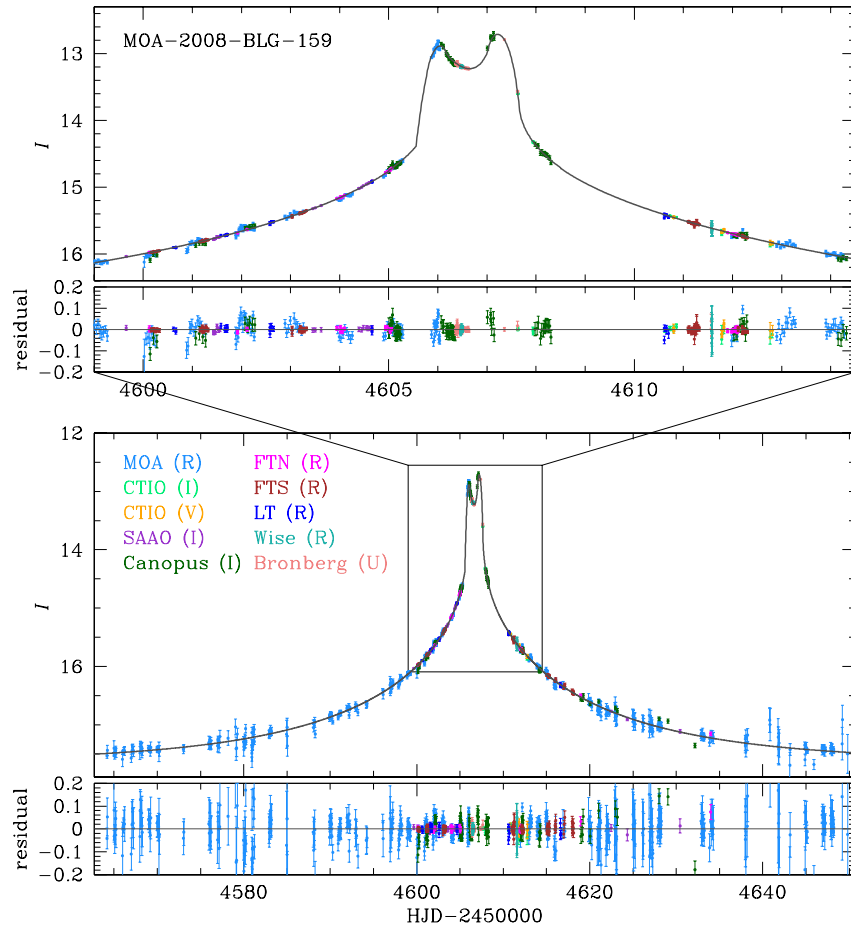
Fig. 2.— Light curve of the microlensing event MOA-2008-BLG-159. Notations same as in Fig. 1.
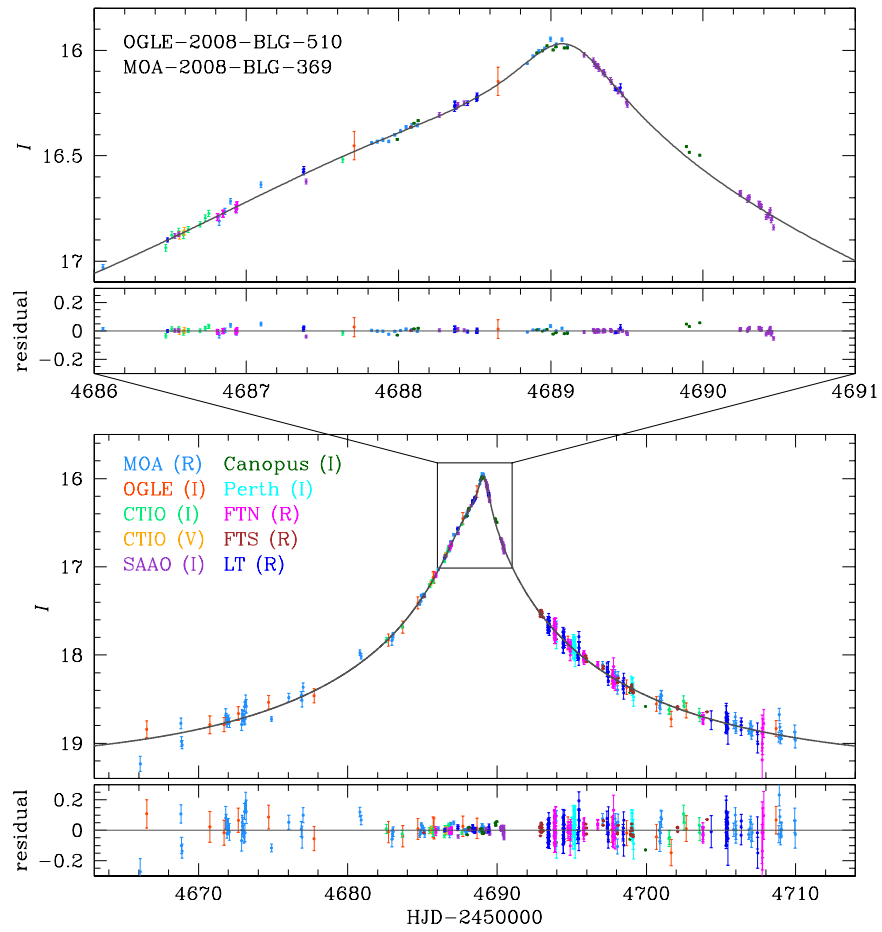
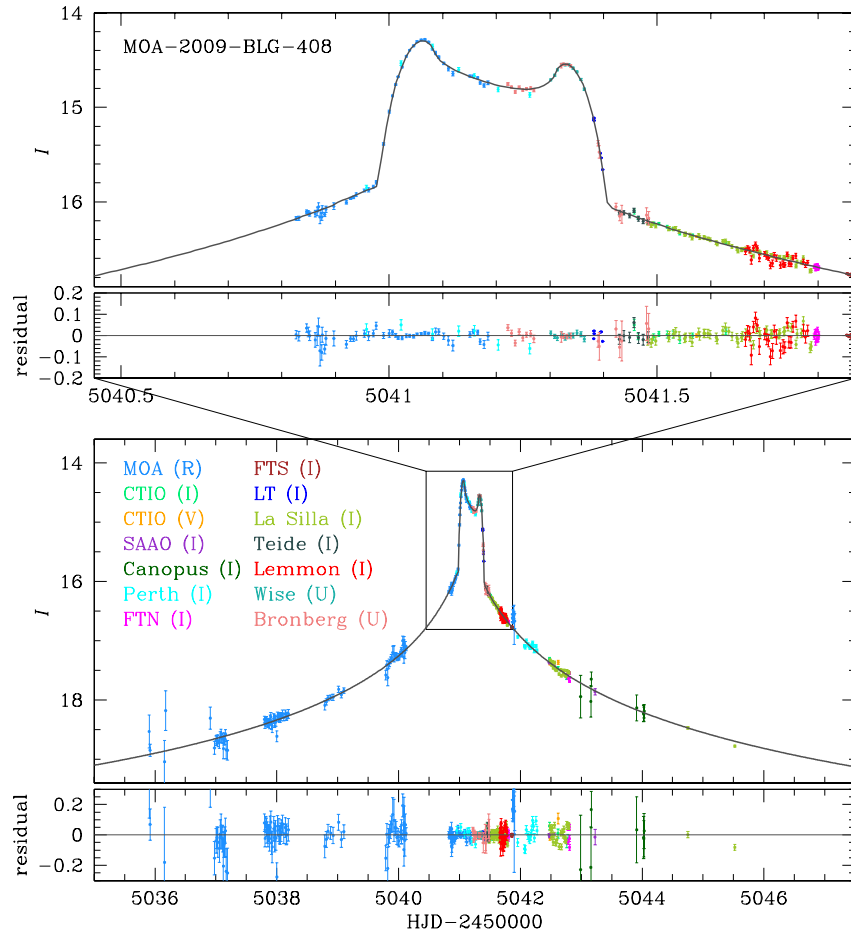Fig. 3.— Light curve of the microlensing event OGLE-2008-BLG-510/MOA-2008-BLG-369. Notations same as in Fig. 1.

Fig. 4.— Light curve of the microlensing event MOA-2009-BLG-408. Notations same as in Fig. 1.

Fig. 5.— Light curve of the microlensing event MOA-2010-BLG-266. Notations same as in Fig. 1.

Fig. 6.— Light curve of the microlensing event MOA-2010-BLG-349. Notations same as in Fig. 1.

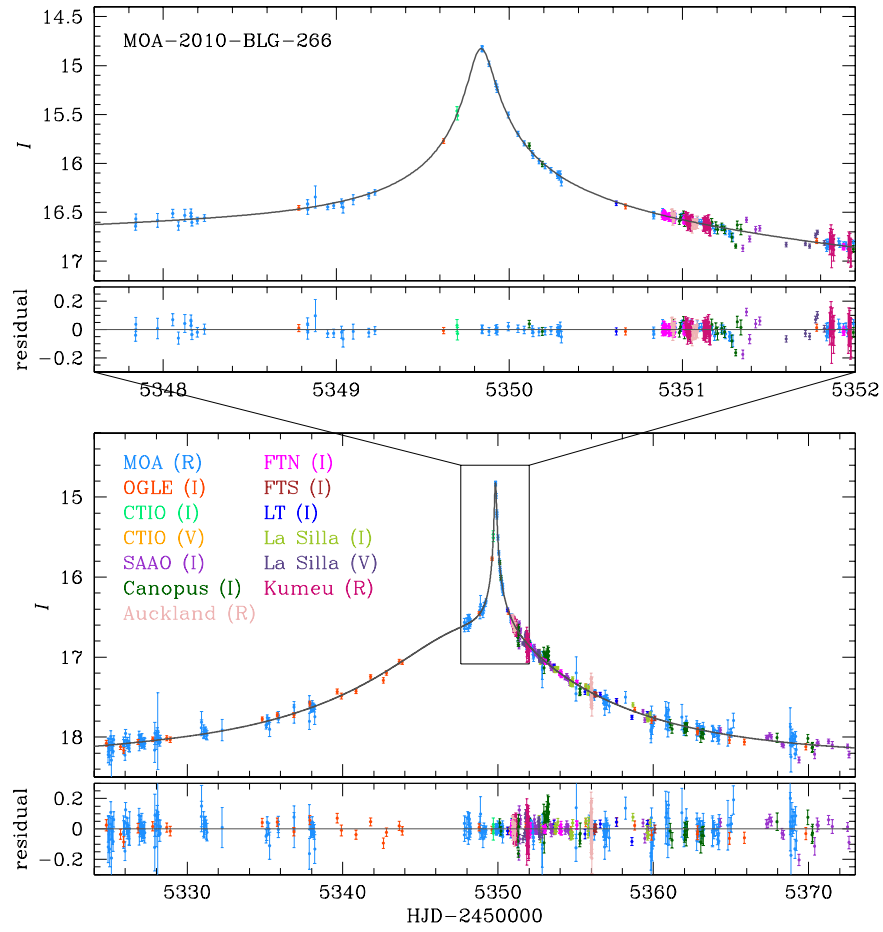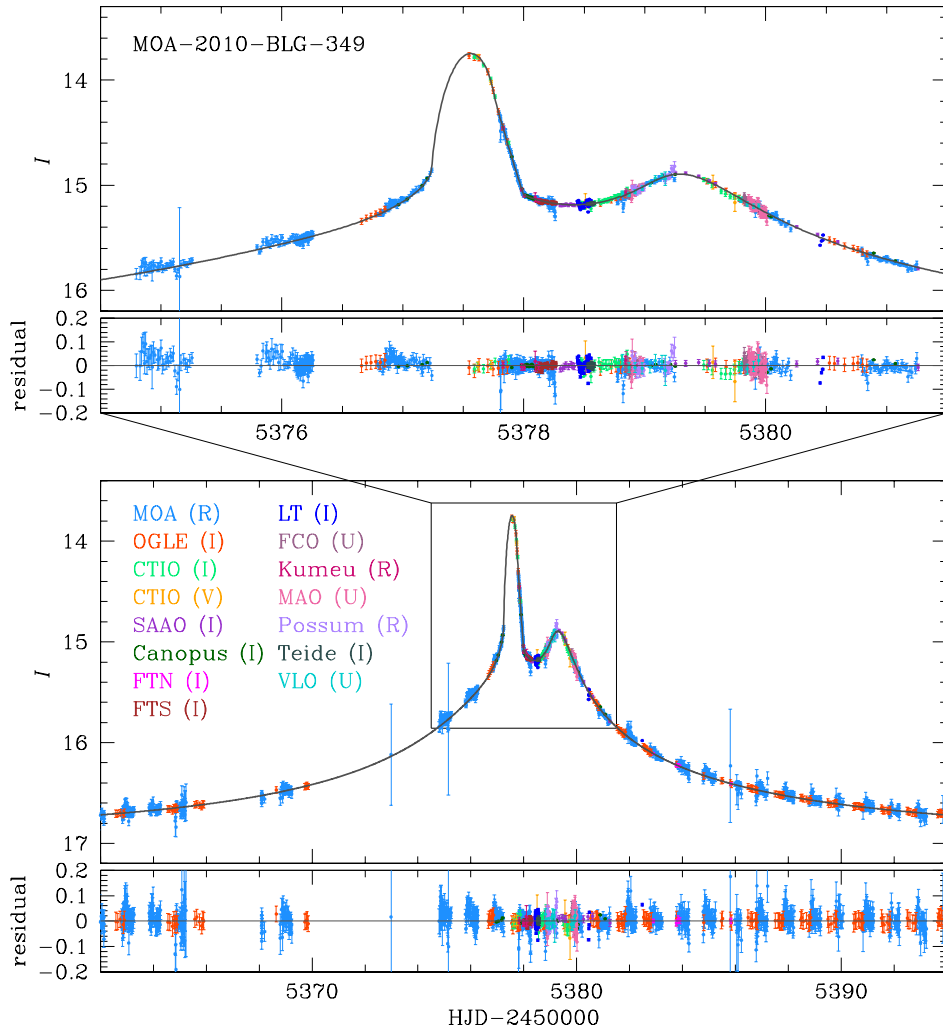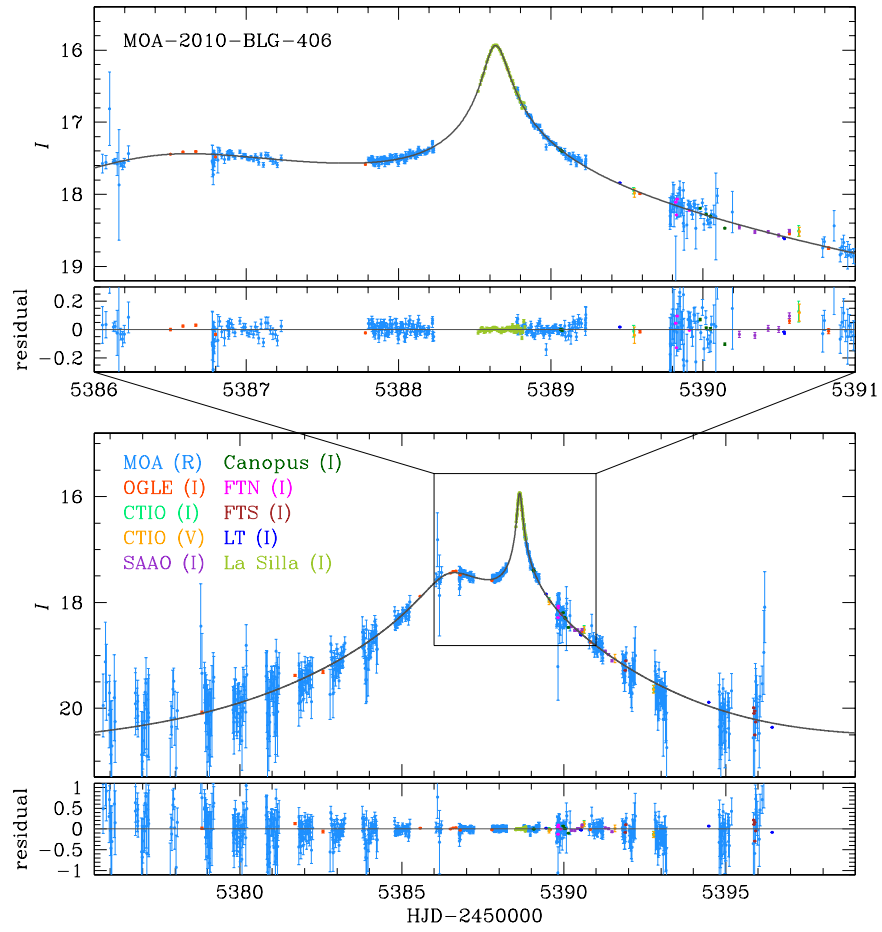Fig. 7.— Light curve of the microlensing event MOA-2010-BLG-406. Notations same as in Fig. 1.
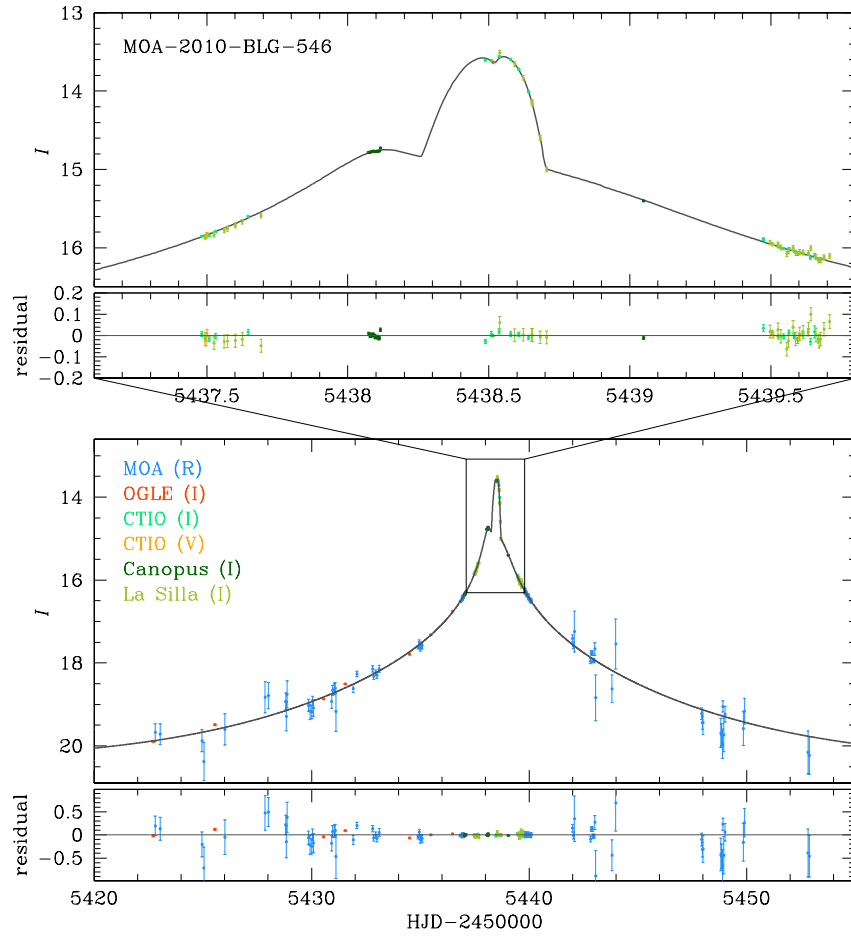
Fig. 8.— Light curve of the microlensing event MOA-2010-BLG-546. Notations same as in Fig. 1.
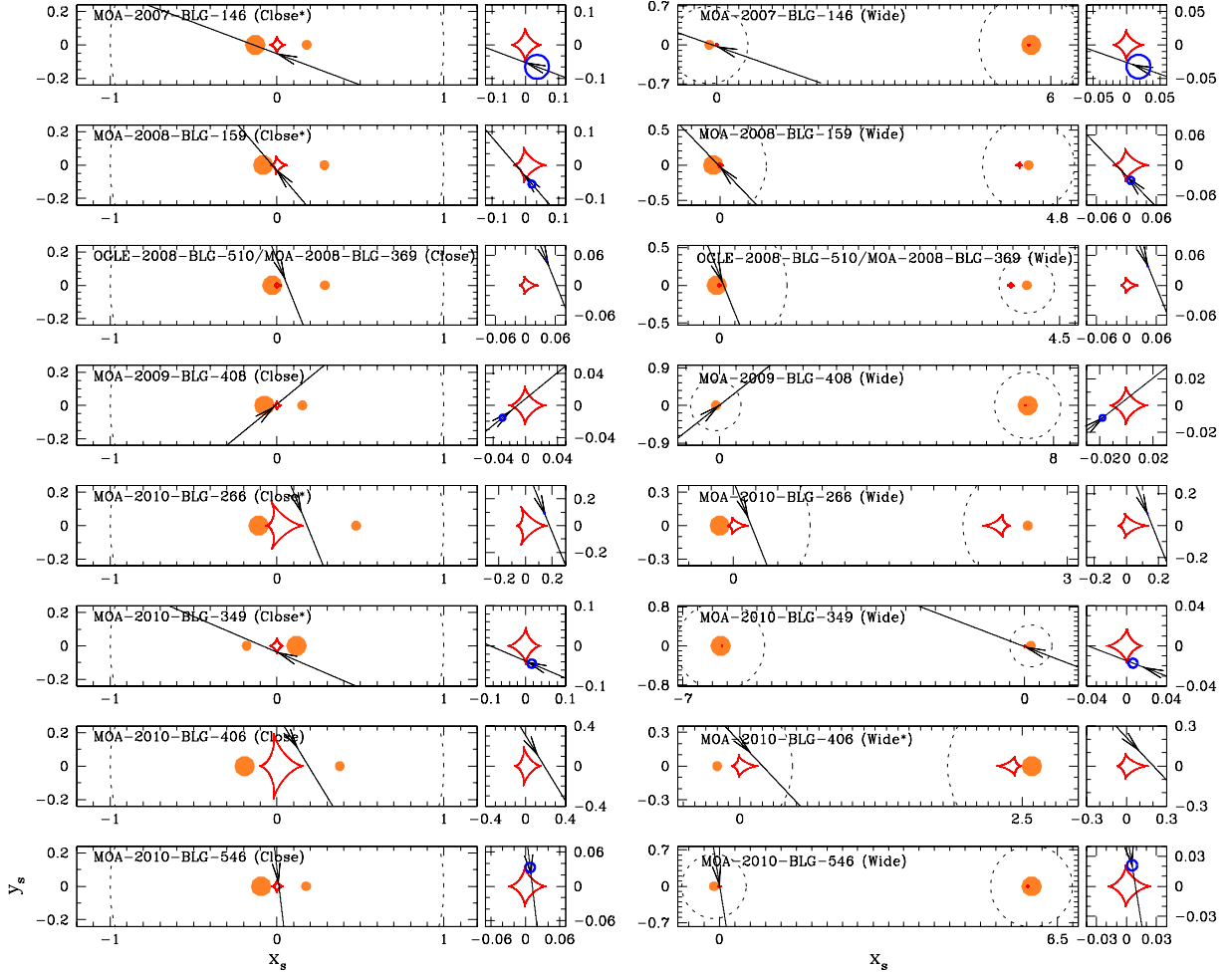
Fig. 9.— Geometry of lens systems responsible for the light curves presented in Fig. 1 – 8. For each event, we present two geometries corresponding to the close (left panels) and wide (right panels) binary solutions. The symbol '∗' after the label 'close' or 'wide' indicates that the model is preferred over the other solution with 3σ level. In each panel, the big and small filled dots represent the lens components with heavier and lighter masses, respectively. The red closed figure represents the caustic and the straight line with an arrow is the source trajectory. The dashed circle represents the Einstein ring. For the close binary, there is a single ring and its radius is the Einstein radius corresponding to the total mass of the binary. For the wide binary, on the other hand, there are two circles with their Einstein radii corresponding to the masses of the individual lens components. The small panel on the right side of each main panel shows the enlargement of the region around the caustic that caused perturbations.
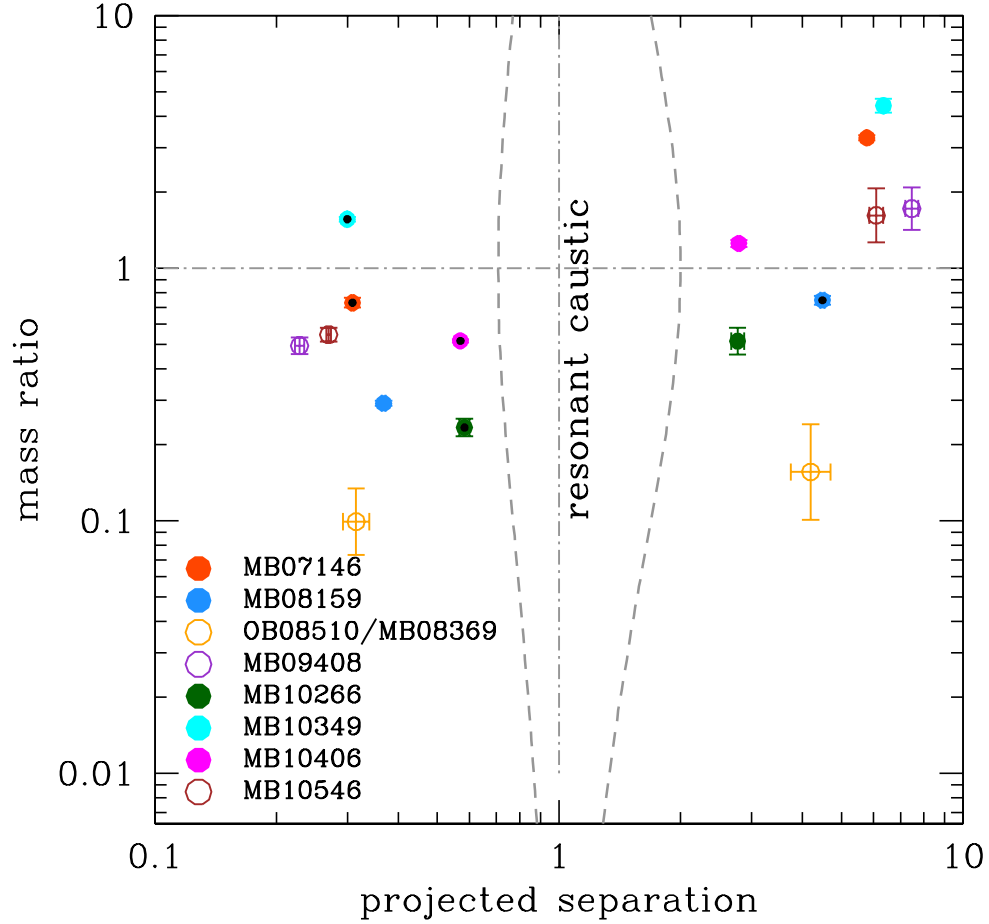
Fig. 10.— Binary solutions in the parameter space of (s, q). The filled circles denote that the degeneracy is resolved with a 3σ confidence level and the empty circles symbolize the degeneracy is not resolved. Among a pair of solutions with resolved degeneracy, we mark a '•' sign inside a circle to indicate which solution is preferred. The area encompassed by dashed lines represents the region within which the lens forms a single merged large caustic.

Table 1: Coordinates of Events

event	RA	DEC	l	b
MOA-2007-BLG-146	$18^h14^m47^s.72$	-27°57'26".9	04°01'59".23	-05°05'03".08
MOA-2008-BLG-159	$18^h07^m29^s.18$	-30°09'49".1	01°19'22".26	-04°43'46".96
OGLE-2008-BLG-510/MOA-2008-BLG-369	$18^h09^m37^s.65$	-26°02'26".7	05°10'23".63	-03°09'32".98
MOA-2009-BLG-408	$17^h57^m08^s.01$	-30°44'18".4	359°43'27".80	-03°04'00".48
MOA-2010-BLG-266	$17^h54^m50^s.84$	-34°15'40".4	356°25'32".88	-04°24'41".22
MOA-2010-BLG-349	$17^h53^m27^s.65$	-28°24'43".3	01°20'01".50	-01°12'20".74
MOA-2010-BLG-406	$17^h55^m27^s.52$	-31°38'55".2	358°45'20".56	-03°12'44".82
MOA-2010-BLG-546	$17^h59^m57^s.69$	-31°35'32".5	359°16'57".50	-04°00'57".13

Table 2: Observatories

event	MOA	OGLE	μFUN	PLANET	RoboNet	MiNDSTEp
MOA-2007-BLG-146	Mt. John		CTIO Auckland CCAO FCO Kumeu Lemmon SSO VLO	Canopus Perth	FTS LT	
MOA-2008-BLG-159	Mt. John		CTIO Wise Bronberg	SAAO Canopus	FTN FTS LT	
OGLE-2008-BLG-510/ MOA-2008-BLG-369	Mt. John	LCO	CTIO	SAAO Canopus Perth	FTN FTS LT	
MOA-2009-BLG-408	Mt. John		CTIO Wise Bronberg Lemmon Teide	SAAO Canopus Perth	FTN FTS LT	La Silla
MOA-2010-BLG-266	Mt. John	LCO	CTIO Auckland Kumeu	SAAO Canopus	FTN FTS LT	La Silla
MOA-2010-BLG-349	Mt. John	LCO	CTIO FCO Kumeu MAO Possum Teide VLO	SAAO Canopus	FTN FTS LT	
MOA-2010-BLG-406	Mt. John	LCO	CTIO	SAAO Canopus	FTN FTS LT	La Silla
MOA-2010-BLG-546	Mt. John	LCO	CTIO	Canopus		La Silla

LCO: Las Campanas Observatory; CTIO: Cerro Tololo Inter-American Observatory; CCAO: Campo Catino Austral Observatory; FCO: Farm Cove Observatory; SSO: Southern Stars Observatory; VLO: Vintage Lane Observatory; MAO: Molehill Astronomical Observatory; SAAO: South Africa Astronomy Astronomical Observatory; FTN: Faulkes North; FTS: Faulkes South; LT: Liverpool Telescope.

Table 3: Telescopes

telescope	location
MOA 2.0 m Mt. John	New Zealand
OGLE 1.3 m Warsaw	Las Campanas, Chile
μFUN 1.3 m SMART	CTIO Chile
μFUN 0.4 m Auckland	New Zealand
μFUN 0.4 m CCAO	Chile
μFUN 0.4 m FCO	New Zealand
μFUN 0.4 m Kumeu	New Zealand
μFUN 1.0 m Lemmon	Arizona
μFUN 0.4 m VLO	New Zealand
μFUN 0.5 m Wise	Israel
μFUN 0.4 m Bronberg	South Africa
μFUN 0.8 m Teide	Canary Islands, Spain
μFUN 0.3 m MAO	New Zealand
μFUN 0.4 m Possum	New Zealand
μFUN 0.3 m SSO	Tahiti
PLANET 1.0 m SAAO	South Africa
PLANET 1.0 m Canopus	Australia
PLANET 0.6 m Perth	Australia
RoboNet 2.0 m FTN	Hawaii
RoboNet 2.0 m FTS	Australia
RoboNet 2.0 m LT	La Palma, Spain
MiNDSTEp 1.54 m Danish	La Silla, Chile

Table 4: Limb-darkening Coefficients

event	Γ_V	Γ_R	Γ_I
MOA-2007-BLG-146	0.74	0.64	0.53
MOA-2008-BLG-159	0.57	0.48	0.40
OGLE-2008-BLG-510/MOA-2008-BLG-369	–	–	–
MOA-2009-BLG-408	0.65	0.56	0.47
MOA-2010-BLG-266	–	–	–
MOA-2010-BLG-349	0.65	0.58	0.48
MOA-2010-BLG-406	–	–	–
MOA-2010-BLG-546	0.68	0.59	0.49

Table 5: Best-fit Model Parameters

event	model	χ^2/dof	t_0 (HJD')	u_0	t_E (days)	s	q	α	$\rho_\star$	$\theta_\star$ (μas)	θ_E (mas)	μ (mas/yr)
MOA-2007-BLG-146	close	1550.7	4249.16	0.049	15.506	0.308	0.729	3.501	0.036	15.512	0.435	10.237
		/1560	±0.004	±0.001	±0.077	±0.002	±0.032	±0.004	±0.001	±1.343	±0.040	±0.932
	wide	1855.6	4249.13	0.053	14.081	5.785	3.279	3.480	0.038	16.013	0.433	10.960
		/1560	±0.003	±0.001	±0.070	±0.025	±0.077	±0.001	±0.001	±1.387	±0.040	±0.998
MOA-2008-BLG-159	close	2407.3	4606.74	0.022	29.180	0.368	0.292	4.006	0.010	1.588	0.156	1.950
		/2418	±0.004	±0.001	±0.343	±0.004	±0.007	±0.004	±0.001	±0.137	±0.020	±0.255
	wide	2472.1	4606.66	0.020	32.221	4.486	0.747	3.947	0.009	1.545	0.169	1.911
		/2418	±0.005	±0.001	±0.379	±0.056	±0.029	±0.004	±0.001	±0.134	±0.022	±0.250
OGLE-2008-BLG-510	close	1879.2	4688.67	0.057	21.531	0.315	0.099	1.191	–	–	–	–
/MOA-2008-BLG-369		/1918	±0.007	±0.002	±0.641	±0.023	±0.030	±0.007	–	–	–	–
	wide	1878.1	4688.65	0.058	21.972	4.100	0.156	1.187	–	–	–	–
		/1918	±0.006	±0.002	±0.654	±0.471	±0.068	±0.008	–	–	–	–
MOA-2009-BLG-408	close	1740.8	5041.20	0.006	13.769	0.228	0.493	5.597	0.004	0.955	0.263	6.975
		/1729	±0.002	±0.001	±0.543	±0.006	±0.037	±0.009	±0.001	±0.083	±0.076	±2.013
	wide	1740.0	5041.20	0.007	13.886	7.472	1.720	5.616	0.003	0.946	0.266	6.994
		/1729	±0.002	±0.001	±0.548	±0.280	±0.332	±0.008	±0.001	±0.082	±0.077	±2.018
MOA-2010-BLG-266	close	4817.0	5348.85	0.167	14.632	0.583	0.234	1.186	–	–	–	–
		/4818	±0.054	±0.008	±0.324	±0.017	±0.019	±0.012	–	–	–	–
	wide	4837.4	5348.70	0.183	15.702	2.768	0.514	1.191	–	–	–	–
		/4818	±0.032	±0.009	±0.348	±0.099	±0.063	±0.013	–	–	–	–

Table 6: Table 5 continued

MOA-2010-BLG-349	close	7883.4	5377.92	0.034	24.695	0.299	1.562	3.546	0.010	4.713	0.458	6.775
		/7946	±0.003	±0.001	±0.193	±0.001	±0.034	±0.002	±0.001	±0.408	±0.060	±0.882
	wide	7909.6	5377.85	0.033	24.530	6.351	4.391	0.365	0.009	4.617	0.443	6.593
		/7946	±0.003	±0.001	±0.192	±0.029	±0.278	±0.002	±0.001	±0.400	±0.058	±0.858
MOA-2010-BLG-406	close	2108.9	5388.13	0.161	5.359	0.570	0.515	1.024	–	–	–	–
		/2030	±0.005	±0.001	±0.057	±0.002	±0.007	±0.004	–	–	–	–
	wide	2020.4	5387.53	0.221	5.362	2.787	1.252	0.815	–	–	–	–
		/2030	±0.007	±0.004	±0.083	±0.018	±0.039	±0.003	–	–	–	–
MOA-2010-BLG-546	close	462.1	5438.49	0.012	8.814	0.269	0.546	1.455	0.008	1.822	0.219	9.082
		/458	±0.003	±0.001	±0.164	±0.004	±0.035	±0.008	±0.001	±0.158	±0.033	±1.347
	wide	458.4	5438.50	0.015	9.305	6.102	1.618	1.411	0.008	1.777	0.214	8.396
		/458	±0.002	±0.001	±0.173	±0.237	±0.398	±0.009	±0.001	±0.154	±0.032	±1.245

$HJD' = HJD - 2450000$. For the wide binary solutions, the lensing parameters u_0 and $\rho_\star$ are normalized by the radius of the Einstein radius corresponding to the mass of the binary lens component that the source trajectory approaches close to. The Einstein time scale, t_E, and the Einstein radius, θ_E, are similarly normalized. We also note that $q < 1$ and $q > 1$ represent the cases where the source trajectory approaches the heavier and lighter lens components, respectively. The Einstein radius is determined by $\theta_E = \theta_\star/\rho_\star$ where the angular radius of the source star $\theta_\star$ is measured based on the source brightness and color. For events where the perturbations do not result from caustic crossings, the values of $\rho_\star$ and θ_E cannot be measured and thus are not presented.